Journal of
Materials Chemistry B

Accepted Manuscript

ROYAL SOCIETY OF CHEMISTRY

www.rsc.org/materialsB

$Ce^{3/4+}$ Cation-Functionalized Maghemite Nanoparticles Towards siRNA-Mediated Gene Silencing

Liron L. Israel[a], Emmanuel Lellouche[b], Ron S. Kenett[c], Omer Green[a], Shulamit Michaeli[b*], and Jean-Paul Lellouche[a]*

[a] *Department of Chemistry & Institute of Nanotechnology & Advanced Materials, Bar-Ilan University, Ramat-Gan, 5290002, Israel.*

E-mail

(Prof. Lellouche): Jean-Paul.M.Lellouche@biu.ac.il

[b] *Faculty of Life Sciences & Institute of Nanotechnology & Advanced Materials, Bar-Ilan University, Ramat-Gan, 5290002, Israel; E-mail(Prof. Michaeli): shulamit.michaeli@biu.ac.il*

[c] *KPA Ltd., Raanana 43100, Israel & University of Turin, Italy*

Pre-formed Massart magnetite (Fe_3O_4) nanoparticles (NPs) have been successfully modified by positively charged lanthanide Ce(III/IV) cations/$[CeL_n]^{3/4+}$ complexes by using a strong mono-electronic Ceric Ammonium Nitrate oxidant (CAN) as Ce donor. The doping process is promoted by high-power ultrasonic irradiation. The reaction has been statistically optimized by Design of Experiments (DoE, MINITAB® 16 DoE software) to afford globally optimized magnetically responsive ultra-small 6.61±2.04 nm-sized CAN_{DOE}-γ-Fe_2O_3 NPs that are highly positively charged (ξ potential: +45.7 mV). This innovative inorganic DoE-optimized NP surface modification by $[CeL_n]^{3/4+}$ complexes enables an effective "fully inorganic-type" coordination attachment of a branched poly-cationic 25kDa b-PEI_{25} polymer for siRNA loading and gene silencing. This innovative NP platform technology paves an efficient way for the successful development of a wide range of biomedicine and diagnostic-relating applications.

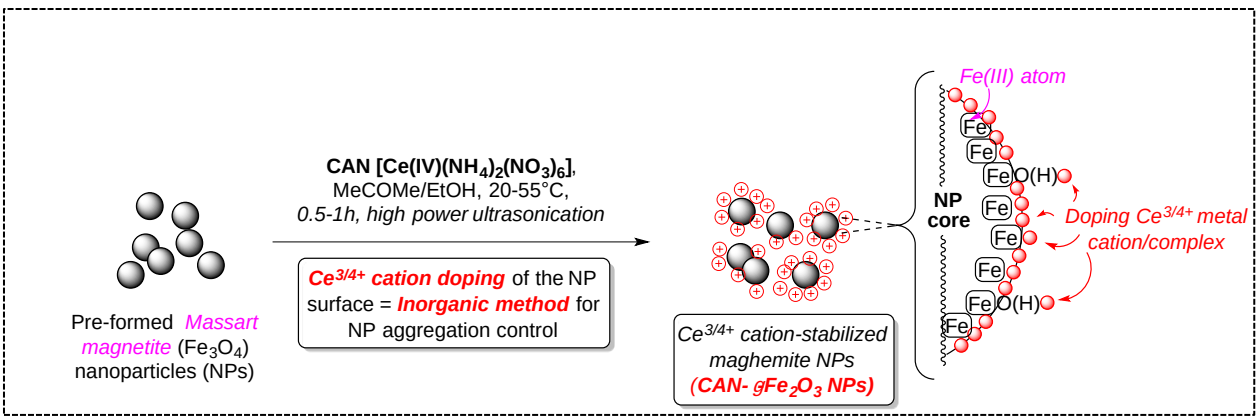

Scheme 1: Overall fabrication of super-paramagnetic CAN-γ-Fe_2O_3 NPs showing NP surface doping $Ce^{3/4+}$ cations

1. Introduction

The ready fabrication of iron oxide-based magnetically responsive NPs and of corresponding functional hybrid organic/inorganic functional composites has strongly stimulated the development of a wide range of biotechnology and nano-medicine related applications. For example, major developments concerned bio-sensing, magnetism-induced cell separation, tracking and drug delivery, nuclear magnetic resonance imaging (MRI), and cancer hyperthermia fields.[1-11] Depending on applications, magnetic composite NPs may be readily prepared and surface-engineered by various functional biocompatible polymeric/co-polymeric (di-block) species.[12] For example, surface passivating species might include both organic and inorganic components, i.e., poly(ethylene glycol)s (PEGs), poly(metha)acrylates (PAs/PMAs), poly-L-lysine (PLL), polyvinylalcohols (PVAs), natural polysaccharides (dextran, chitosan and poly alginic/hyaluronic acids), dendrimers (PAMAMs) of various generations, cyclodextrins, proteins (human and bovine serum albumins), hydrophobic bifunctional NP capping lipid species (oleyl amine/acid mixtures), inorganic silica (SiO_2) corona phases, and corresponding hybrid variants. This non-exhaustive list of NP surface modifying species rather emphasized the critical importance of an optimal application-oriented NP surface engineering. Clearly, a reasonable NP design and surface engineering should address highly important issues, - the minimization of potentially detrimental NP aggregation, as well as a ready access to versatile NP surface chemistries for second step functionalization.

In this context, we recently disclosed the preparation of highly hydrophilic 10-15 nm (TEM)/50-60 nm (hydrodynamic diameter by DLS- Dynamic Light Scattering)-sized super-paramagnetic maghemite (γ-Fe_2O_3) NPs. The resulted NPs were highly stable aqueous suspensions/ferrofluids due to a unique ultrasound-mediated doping process of the NP surface using lanthanide $Ce^{3/4+}$ cations (Scheme 1).[13] This innovative NP surface engineering process makes use of a high-power oxidative ultra-sonic irradiation of pre-formed partially aggregated 10-15 nm-sized Massart magnetite (Fe_3O_4) NPs. Magnetite NPs were then reacted with a strong mono-electronic oxidant, Ceric Ammonium Nitrate [CAN, $Ce^{IV}(NH_4)_2(NO_3)_6$, 1/1 v/v MeCOMe/H_2O, 20-55°C, Ar atmosphere).[14-16] It provides highly positively charged hydrophilic super-paramagnetic CAN-stabilized γ-Fe_2O_3 NPs (CAN-γ-Fe_2O_3 NPs). CAN-γ-Fe_2O_3 NPs commonly disclosed ξ potentials in a +40.0 - +43.0 mV range that enables effective control of NP aggregation (electrostatic NP repulsive interactions) in aqueous media.

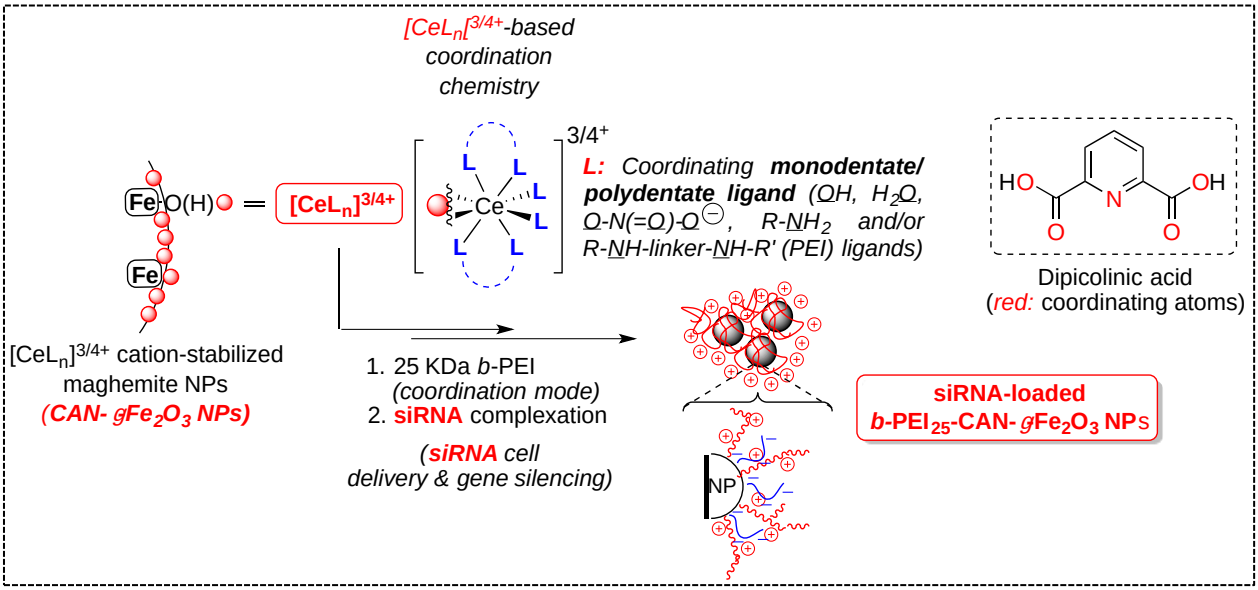

Scheme 2: $[CeL_n]^{3/4+}$ cation-mediated functionalization of CAN-γ-Fe_2O_3 NPs by (i) a polycationic 25kDa branched PEI polymer (b-PEI) and (ii) siRNA species for cell delivery/gene silencing - siRNA-loaded ultra-small b-PEI-containing $Ce^{3/4+}$-doped maghemite (γ-Fe_2O_3) nanoparticles (siRNA-loaded b-PEI_{25}-CAN-γ-Fe_2O_3 NPs)

Being CAN-specific, this anti-aggregation effect of the $Ce^{3/4+}$ cation doping process did not result from the common formation of any inorganic CeO_2 shell.[13] It has been rather rationalized by the likely formation of surface-localized Fe(III)-O-$Ce^{3/4+}L_n$ species (Scheme 2, L: $Ce^{3/4+}$ cation coordinating ligands, - NO_3- anions and/or H_2O/OH groups) in addition to the high-energy ultra-sound-promoted formation of Ce/Fe atom-relating surface defects (atom vacancy filling and/or replacement). Moreover, extensive combined ICP-AES and TEM-EDAX measurements demonstrated that these CAN-γ-Fe_2O_3 NPs possessed an astonishingly low level of surface doping by $[CeL_n]^{3+}$ complex cations (Ce EDAX element assays: 0.24 wt%, 0.02 atom%).[13]

Beyond the powerful capability of this innovative inorganic way to electrostatically control CAN-γ-Fe_2O_3 NPs aggregation, the present study focused on another challenging under-estimated aspect - NP surface functionalization/engineering for siRNA/microRNA cell delivery and gene silencing applications. On the basis of the known rich $[CeL_n]^{3/4+}$-complex ligand coordination chemistry,[17-21] can the NP surface doping $[CeL_n]^{3/4+}$ complexes enables successful coordinative attachment of any Lewis base N/S/O-containing organic species via L ligand exchange towards corresponding functionalized NPs? Strongly electropositive $[CeL_n]^{3/4+}$ complexes belong to the tri/tetravalent lanthanide cationic complex family and can readily react as hard Lewis acid towards mono and polyvalent organic species. For example, it is known that small mono-dentate coordinating anions preferably react with trivalent lanthanide cations according to the following electronegativity (hardness) order F- > OH- > H_2O > NO_3-> Cl- with a maximal coordination number of six to nine depending on cation size.[20, 21]

Therefore, a NP surface decoration methodology that will rely on shell coordination-enabling $[CeL_n]^{3/4+}$ complexes will need to significantly increase their overall surface amount to be effective for NP functionalization. This will likely promote optimal binding

and/or chelating interactions with Lewis base mono and multi-dentate ligands including chelating polymers like a poly-cationic endosomolytic 25kDa branched b-PEI polymer. If successful, this corresponding NP surface functionality engineering will not use any organic bifunctional linker for NP functionalization towards innovative poly-cationic hybrid core (CAN-γ-Fe_2O_3)-shell (b-PEI) magnetic nano-carriers (NCs). For that purpose, this study will provide solid evidence that resulting functional NCs might be optimally designed using a statistically significant Design of Experiments (DoE) method[22-25] towards highly effective siRNA/microRNA electrostatic capture and stabilization, cell delivery, and gene silencing.

2. Results and Discussion

2.1. Key observation - [$Ce^{3/4+}L_n$] complex coordination capabilities

Importantly and before any DoE optimization work, this conceptually novel NP functionalization approach has been first validated by a key simple "saturation" experiment. This experiment aimed at checking the potential effectiveness of surface-localized [$Ce^{3/4+}L_n$] species to complex a poly-cationic 25kDa branched b-PEI polymer. For that purpose, former 10.0-15.0-sized CAN-γ-Fe_2O_3 NPs (3.20 mg NPs, 1.77 mg elemental Fe/ICP-AES) have been first contacted with dipicolinic acid in excess (Dpic, Scheme 2, 0.1 mg, 0.598 µmol, ddH_2O, 3 days, 20°C) to afford corresponding Dpic-modified CAN-γ-Fe_2O_3 NPs (cleaning step: sequential centrifugal NP precipitation-re-dispersion, ddH_2O washing, x3). Dpic possesses three coordinating (H)O/C=O/N atoms (tridentate ligand) that enable effective chelating complexation of $Ce^{3/4+}$ cations.[20, 26, 27] As expected due to the readily ionized bis-acidic Dpic structure, Dpic-modified CAN-γ-Fe_2O_3 NPs disclosed both a reduced ξ potential (+34.2±0.61 mV) and a slightly increased particle size (DLS: 64.41±0.25 nm) in comparison to starting CAN-γ-Fe_2O_3 NPs. Then, same Dpic-modified CAN-γ-Fe_2O_3 NPs (0.2 mL, 0.70 mg elemental Fe/ICP-AES) have been similarly contacted with an exact excess amount of fluorescent FITC-labeled 25KDa b-PEI polymer (FITC-b-PEI_{25}/DMSO, 0.12 mg, 0.0048 µmol, ddH_2O, overnight, 20°C) prepared according to Kim J. H. et al.[28] Extensive cleaning of resulting NPs (sequential centrifugal precipitation & NP re-dispersion, ddH_2O washings, x3) afforded a pooled aqueous washing phase that exactly fitted the initial amount of FITC-b-PEI engaged in this "surface saturation" experiment (UV absorption quantification using FITC fluorescence signal, λmax = 495 nm, extinction coefficient: 75,000 M-1cm-1).[29] This enabled to conclude that the FITC-b-PEI_{25} polymer was unable to bind Dpic-modified CAN-γ-Fe_2O_3 NPs most likely because of the 1st step formation of "saturation" [$Ce^{3/4+}$-$Dpic_3$] complexes.

2.2. Design of Experiment (DoE)-improved $Ce^{3/4+}$ cation doping process - Fabrication of new DoE-optimized CAN_{DOE}-γ-Fe_2O_3 NPs

Since the functionalization level of the NP surface by doping $Ce^{3/4+}$ cations/[$Ce^{3/4+}L_n$] complexes has a critical importance regarding coordination capability and delivery of corresponding optimally surface engineered NPs, a statistically designed experiment (DoE)[22-25] has been implemented. It aimed at disclosing an optimal set of NP fabrication conditions that would result in the obtainment of a maximized reproducible level of NP surface doping by $Ce^{3/4+}$ cations/[$Ce^{3/4+}L_n$] complexes toward both DoE-globally optimized core CAN_{DOE}-γ-Fe_2O_3 and related b-PEI-functionalized b-PEI-CAN_{DOE}-γ-Fe_2O_3 NPs. Such a DoE study will enable to modify more than one factor/reaction condition at a time for process optimization even when involving numerous influential factors. Moreover, it will enable to

run fewer experiments. This approach will also enable to study how reaction factors interact with each other and how such interaction will influence on final results, which is unavailable using more commonly used (one factor at a time) OFAT optimization studies.

Run order	**Ageing time** (h)	**CAN oxidant** (mg)	**Solvent component - MeCOMe volume** (mL)	**Ultra-sonication time** (h)
1	12	150	6	0.5
2	2	500	18	1.5
3	12	500	6	0.5
4	2	500	6	0.5
5	2	150	6	0.5
6	**7**	**325**	**12**	**1**
7	12	500	6	1.5
8	12	500	18	0.5
9	2	500	18	0.5
10	2	150	6	1.5
11	12	150	18	0.5
12	12	150	6	1.5
13	2	150	18	1.5
14	2	500	6	1.5
15	12	500	18	1.5
16	12	150	18	1.5
17	2	150	18	0.5

[a] Experimental array of DoE-optimized core CAN_{DOE}-γ-Fe_2O_3

For this purpose and based on our current process knowledge, four main factors (reaction parameters) that might significantly affect the doping process have been identified (Table 1 & SI, section B, illustrative experimental doping protocol). Being set-up at both low and high value levels, these investigated factors are (i) the ageing time of the starting magnetite (Fe_3O_4) NPs (time between magnetite NP preparation and CAN-mediated ultrasound-assisted doping step, two values: 2 & 12h), (ii) the CAN oxidant amount (two values: 150.0 & 500.0 mg), (iii) the volume of the MeCOMe solvent component at a total constant reaction H_2O/MeCOMe volume of 24.0 mL (two values: 6.0 & 18.0 mL), and finally the high-power ultra-sonication time at a fixed 25% modulator power (Sonics®, Vibra cell/Ti horn, 750 Watt; two values: 0.5 & 1.5h). Thus, a four factor-two level full factorial experimental array was designed and analysed using the MINITAB® 16 DoE software (version 16.2.4, Minitab Inc.). The design included one factor replicate (one repetition of the experiments) and one center point (Table 1, St. order 6). That experimental array consists of a total of 17 (16 + 1 center point, 1 block) experiments (Table 1) that have been randomized in order to remove possible time related confounding effects. These experiments provided quantified responses (reaction outcomes), i.e., (i) the average DLS hydrodynamic size of resulting CAN_{DOE}-γ-Fe_2O_3 NPs with polydispersity indexing (PDI), (ii) their average TEM size and distribution (analysis of more than 100 objects, J Image software), (ii) their ξ potential, (iii-iv) both normalized Ce and Fe elemental weight suspension contents, and finally (v) prime importance NP w/w elemental Ce/Fe ratios (Table 2).

St. Order	**DLS size** (nm)	**PDI**	**TEM size** (nm)	**ζ Potential** (mV)	**Ce** (mg/mL)	**Fe** (mg/mL)	**Ce/Fe w/w ratio**
1	49.65	0.172	7.470	+33.0	0.0250	3.4500	0.00725
2	54.05	0.192	6.827	+40.5	0.0579	3.6920	0.01568
3	55.56	0.117	6.989	+52.1	0.2230	2.8900	0.07716
4	45.72	0.144	6.813	+47.2	0.2050	3.2890	0.06230
5	49.05	0.187	6.486	+37.6	0.0239	3.6650	0.00652
6	**37.04**	**0.134**	**7.630**	**+37.1**	**0.0765**	**3.4800**	**0.02198**
7	40.81	0.162	7.852	+33.6	0.1580	3.4200	0.04620
8	80.20	0.173	8.100	+47.3	0.0868	3.8300	0.02266
9	56.64	0.175	7.599	+30.9	0.1060	3.4730	0.03052
10	34.78	0.213	7.610	+26.3	0.0041	3.4150	0.00120
11	84.08	0.141	8.001	+34.9	0.0242	4.0900	0.00592
12	40.93	0.157	7.403	+35.4	0.0230	4.0700	0.00565
13	58.88	0.172	6.786	+39.9	0.0163	3.8310	0.00425
14	38.37	0.180	7.018	+46.4	0.1630	3.2790	0.04971
15	51.80	0.143	7.711	+50.4	0.2160	4.1100	0.05255
16	75.73	0.169	7.683	+35.0	0.0115	3.7800	0.00304
17	65.87	0.134	7.424	+23.2	0.0233	3.1640	0.00736

[a] Experimental array (core CAN_{DOE}-γ-Fe_2O_3) and corresponding process responses.

First, response analyses that characterized the experimental array under investigation indicated that all the NPs obtained were strongly positively charged in a +23.2 - +52.1 mV range of ξ potential values (Table 2, St. orders 17 vs. 3). These data are indicative of an overall successful doping process by $Ce^{3/4+}$ cations/[$Ce^{3/4+}L_n$] complexes. Moreover and amongst all four investigated factors, the most influential one that afforded a corresponding optimal maximized w/w Ce/Fe ratio (Table 2, St. order 3, w/w Ce/Fe ratio: 0.07716) has been shown to be the CAN oxidant amount using a Pareto chart of standardized effects (Fig. 1 - top, significance α-level set-up at 0.05). In the Paretto chart, the only response that crossed the red line, meaning being statistically significant in influencing the Ce/Fe ratio was the CAN oxidant amount.

Interestingly, such a high-level w/w Ce/Fe ratio measured at St. order 3 was found to be much higher than the one measured for former non-optimized core CAN-γ-Fe_2O_3 NPs by a 266.1% factor, thus validating this DOE approach for global optimization. All other primary and interactive secondary/tertiary order standardized effects were less significant.

Both CAN oxidant (Fig. 1 - top, secondary order BC interaction) and MeCOMe amounts (Fig. 1 - top, primary C factor) showed effects of high magnitude. The corresponding 2D contour plots of w/w Ce/Fe ratios and TEM NP sizes vs. both CAN oxidant and MeCOMe amounts are reported in Figures 1 (bottom) and SI-1 (SI, p. SI-5) respectively. This analysis disclosing graphs similar to topographic maps showed two amongst reaction factors using both axes X & Y, while the chosen response is color-encoded at Z axes.

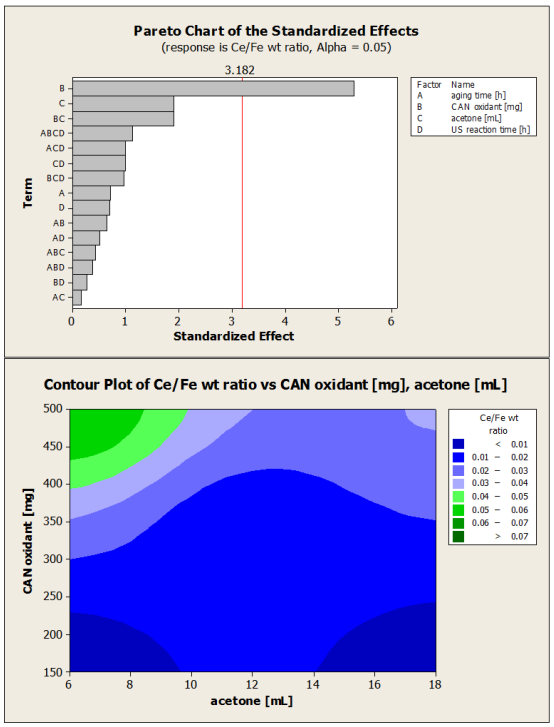

Figure 1: DoE-optimized fabrication of CAN_{DOE}-γ-Fe_2O_3 NPs – Pareto chart of standardized effects for the response w/w Ce/Fe ratio (top) & 2D contour plot of w/w Ce/Fe ratios vs. CAN oxidant (mg) & MeCOMe (mL) amounts (bottom)

Importantly, the 1st contour plot graph (Fig. 1, bottom) indicated that highest 0.06-0.07-ranged w/w Ce/Fe ratio values have been obtained for a (i) 6.0 mL MeCOMe volume and (ii) CAN oxidant amount greater than 430.0 mg and higher. The 2nd contour plot (Fig. SI-1) also validated such similar CAN oxidant/MeCOMe-relating conditions in order to obtain the smallest 7.0-7.25 nm range of NP sizes. This same set of conditions also afforded NP highest ξ potential and smallest hydrodynamic size (DLS) values (+40 - +45 mV & 40-50 nm domains, 2D contour plots - Figs. SI-2/p. SI-5 & SI-3/p. SI-6 respectively).

In order to better identify significant factor interactions, full matrices of two-way interaction plots that related to NP size (TEM) and ξ potential factors have been generated as shown in Figure 2 - top & bottom respectively. An interaction plot basically reveals if there is an interaction between two different factors/reaction conditions for a certain response. When the two considered graphs are either super-imposed or parallel, it means that there is no interaction between these two factors. On the contrary, line intersection indicates a strong interaction between these two considered factors. From graph examination (red spot: center point), several interesting conclusions might be drawn. For example, both MeCOMe volume and high-power ultra-sonication time factors disclosed significant interactions for NP size (TEM) and ξ potential responses (Fig. 2 - top & bottom respectively).

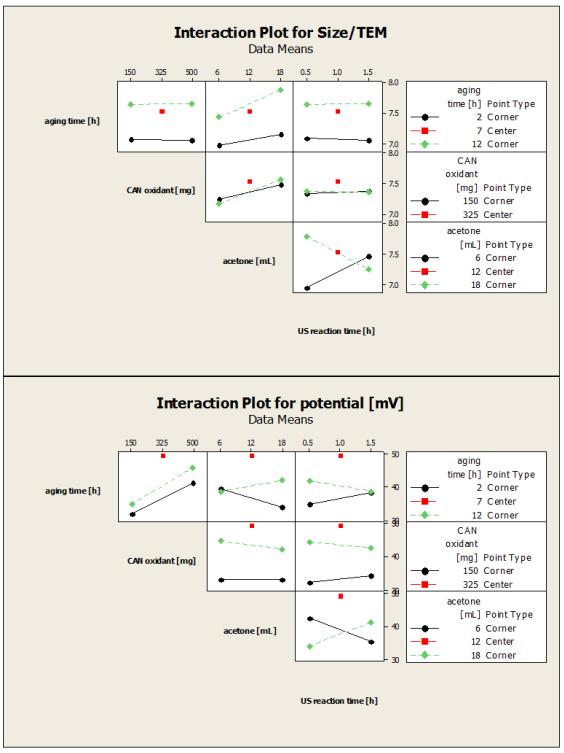

Figure 2: DoE-optimized fabrication of CAN_{DOE}-γ-Fe_2O_3 NPs - Full interaction plot matrices for both NP size (TEM, top) & ξ potential (bottom) factors

Concerning the NP size (TEM) response, the magnetite NP ageing time factor did not show any interaction with both (i) CAN oxidant amount, and (ii) high-power ultrasonication time (Fig. 2 - top). Moreover, moderate interactions between (i) magnetite NP ageing time and MeCOMe volume factors (Fig. 2 - top), and (ii) magnetite NP ageing time and high-power ultra-sonication time factors (Fig. 2 - bottom) have been also evidenced for both NP size (TEM) and ξ potential factor responses respectively.

2.3. Nanoparticle surface engineering refinement - Use of the MINITAB® 16 software profile optimizer tool

The clear interacting multi-parametric character of the overall NP fabrication process necessitated to "engineer and refine" an optimal setting of input factors for the delivery of most optimized surface attachment-enabling core CAN-γ-Fe_2O_3 NPs. For this purpose, the MINITAB® 16 software profile optimizer tool has been used. This tool allows to select a target set of parameter values (lower to higher ones) toward a quite precise overall response. Then, both lowest or highest acceptable factor limits enables to rank each response according to its level of importance (from the lowest, i.e., 1 to the highest one, i.e., 10). The following specifications were set (Fig. SI-4, p. SI-6): the elemental w/w Ce/Fe ratio has been selected as the most important input factor for process optimization, i.e., choosing a selected level 4 of importance with both lower and target response values of 0.05 and 0.1 respectively. Then, other input factors have been classified and adjusted according to the following order of importance, - (i) the NP size (TEM, level 3; target and upper limit values: 6.5 & 7.5 nm), (ii) the NP ξ potential (level 2, lower limit and target values: +40 - +50mV), and finally (iii) the NP hydrodynamic size (DLS, level 1, target and upper limit values: 40.0 & 50.0 nm). The corresponding calculated optimization plot has been reported in Fig. 3 (red data/red current line) and disclosed the effect of each factor (columns) on corresponding responses and response desirabilities (right column, blue data). In this case, this software optimizer tool suggested the use of a 4.22h ageing time for starting magnetite NPs, 500.0 mg of CAN oxidant, 6.0 mL of MeCOMe, and 0.5h high-power ultra-sonication time for the obtainment of globally optimized CAN_{DOE}-γ-Fe_2O_3 NPs. These NPs should possess the following calculated physico-chemical characteristics: (a) a minimized NP hydrodynamic size (DLS) of 47.21 nm, (b) a maximized ξ potential of +50.05 mV, (c) a maximized w/w Ce/Fe ratio of 0.0634, and (d) a minimized NP TEM size of 6.88 nm.

Therefore, these calculated optimizer set of reaction conditions have been used for the corresponding NP fabrication (Section SI-B, p. SI-2). They afforded corresponding DOE-optimized CAN_{DOE}-γ-Fe_2O_3 NPs that possessed the following physico-chemical properties, i.e., (a) a NP hydrodynamic size (DLS) of 60.00 nm (Fig. SI-5 p. SI-7), (b) a positive ξ potential of +45.7 mV, (c) a w/w Ce/Fe ratio of 0.1000 that was higher that the software prediction by a 60.5% factor, and (d) a slightly smaller NP TEM size of 6.61±2.04 nm (Fig. 4 bottom-right). The first two experimental NP features were found quite close to the corresponding software optimizer predicted values mentioned above while the two last ones have been even better when compared to same profile optimizer predicted values. Interestingly, all these core NP characterization data have been also readily reproduced

without any significant data deviation (< 1.0%) for numerous NP batch preparations.

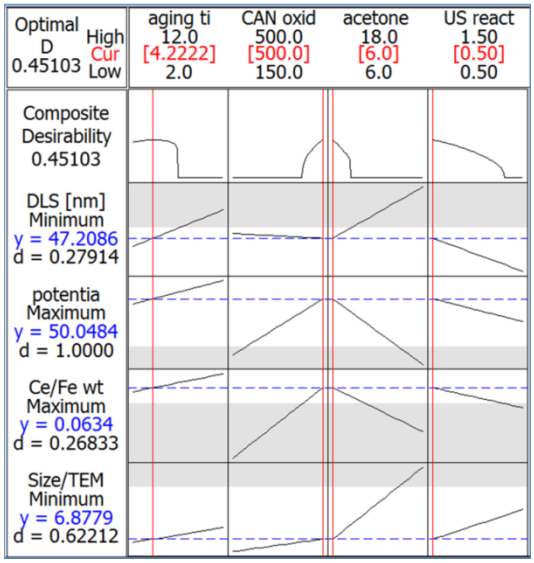

Figure 3: DoE-optimized fabrication of CAN_{DOE}-γ-Fe_2O_3 NPs - Calculated optimization plot (red data/red current line) using the MINITAB® 16 software profile optimizer tool

2.4. DoE-optimized CAN_{DOE}-γ-Fe_2O_3 NPs - characterization data

At this stage of core NPs developmental studies, these optimized CAN_{DOE}-γ-Fe_2O_3 NPs have been further characterized by various combined analytical, spectroscopic and microscopy methods. For example, TEM (Fig. 4, top-left & Fig. SI-5, p. SI-7) and high-resolution TEM (HR-TEM, Fig. 4, top-right) microphotographs indicated the formation of well-shaped spherical crystalline (lattice fringes observation) and non-aggregated NPs. NP crystallinity has been further confirmed by both TEM/Selected-Area Electron Diffraction (SAED) pattern and powder X-ray diffraction (XRD) analyses (Fig. 4, top-middle & Fig. 5 respectively). Both analyses clearly emphasized the four most significant individual (220, 2θ: 30.266°), (311, 2θ: 35.651°), (400, 2θ: 35.651°), & (440, 2θ: 62.949°) diffraction planes that characterized a typical spinel crystalline maghemite/magnetite phase (JCPDS card n° 39-1346). More importantly, the DoE-optimized doping level by cationic $[CeL_n]^{3/4+}$ complexes reached a very high level (w/w Ce/Fe ratio of 0.1000) compared to former non-optimized CAN-γ-Fe_2O_3 NPs that both HR-TEM/compositional EDAX (Fig. 4, bottom-left) and surface-sensitive X-ray photoelectron spectroscopy (XPS, Fig. 6) analyses unambiguously detected. XPS detected the presence of (i) NP surface-localized doping $[Ce^{3/4+}L_n]$ species (Ce $3d_{5/2}$ peak, binding energy (BE): 890.47 eV), and of (ii) NP surface complexing nitrate anions (N 1s peak, L: complexing NO_3-, BE: 407.39 eV, NIST X-ray Photoelectron Spectroscopy Database/Web site: http://srdata.nist.gov/xps/Default.aspx). These combined data have been also strengthened by FT-IR spectroscopy that provided clear evidence that both coordinating nitrate (NO_3-) anions and H_2O

molecules have been adsorbed onto the NP surface via [$Ce^{3/4+}L_n$] complex coordination (Fig. SI-6, p. SI-7). Indeed, both 1352.92 and 1553.49 cm-1 FT-IR absorption peaks might be readily assigned to a n_3 degenerated mode of vibrations for NO_3- and solvated NO_3- anions respectively, - their n_1 mode of vibrations being detected at 1042.16 cm-1.[30]

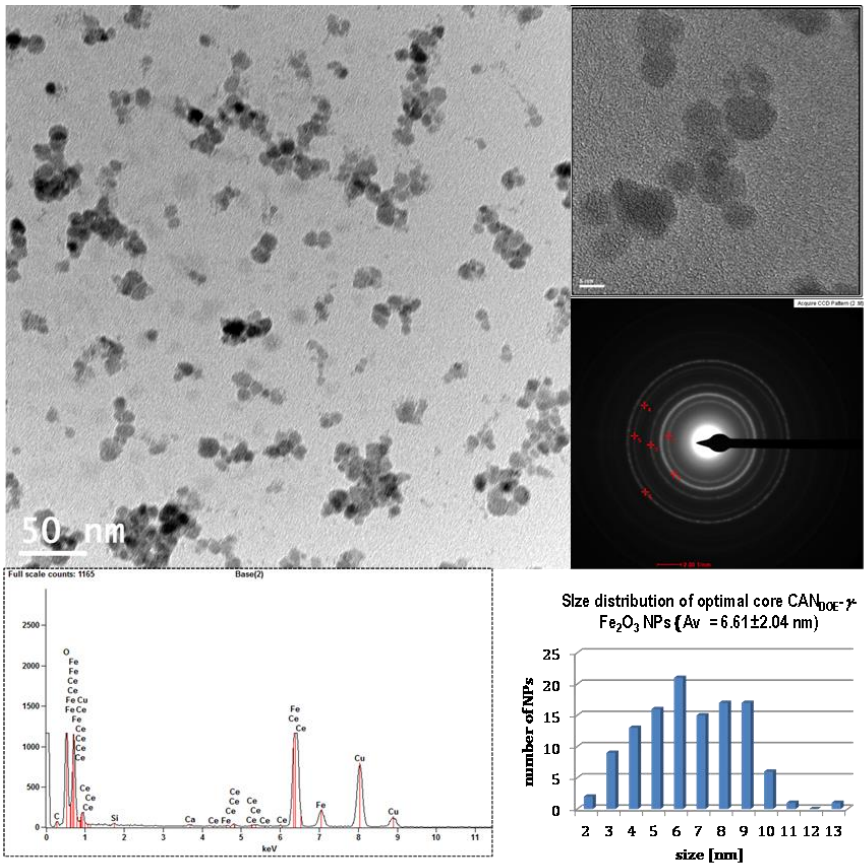

Figure 4: TEM (top-left, scale bar: 50 nm) & HR-TEM (top-right, scale bar: 5 nm) microphotographs of ultra-small 6.61±2.04 nm-sized core CAN_{DOE}-γ-Fe_2O_3 NPs with TEM/Selected Area Electron Diffraction (SAED) patterns (top-medium): #1 (plane 220), #2 (plane 311), #3 (plane 400), & #6 (plane 440) , compositional EDAX analysis (bottom left) showing the presence of both Fe & Ce elements & size distribution histogram of ultra-small 6.61±2.04 nm-sized core CAN_{DOE}-γ-Fe_2O_3 NPs (MINITAB® 16 software profile optimizer tool output, TEM microphotograph analysis, bottom right)

Moreover and due to the chemical reactivity of surface [$Ce^{3/4+}L_n$] complexes, CAN_{DOE}-γ-Fe_2O_3 NPs (0.85 mg, 1.0 mL ddH_2O) have been successfully surface-modified with 1,4-diaminobutane in excess (H_2N-$(CH_2)_4$-NH_2, 0.2 mL, 2.58 mmol, overnight, 20°C, SI-B section, p. SI-3) for quantitative Kaiser testing.[31] As expected, this short linear 1,4-diamine acted as a Lewis base coordinating species for $[CeL_n]^{3/4+}$ complexes (experimental details, SI-B section, p. SI-3) to afford corresponding polyNH_2-modified CAN_{DOE}-γ-Fe_2O_3 NPs. Then, outer primary NH_2 groups (coordinated polyNH_2 shell) have been assayed using a sensitive ninhydrin-based UV spectrophotometric test (triplicate format) that afforded an average value of 0.272±0.023 µmol accessible NH_2 groups/mg CAN_{DOE}-γ-Fe_2O_3 NPs.

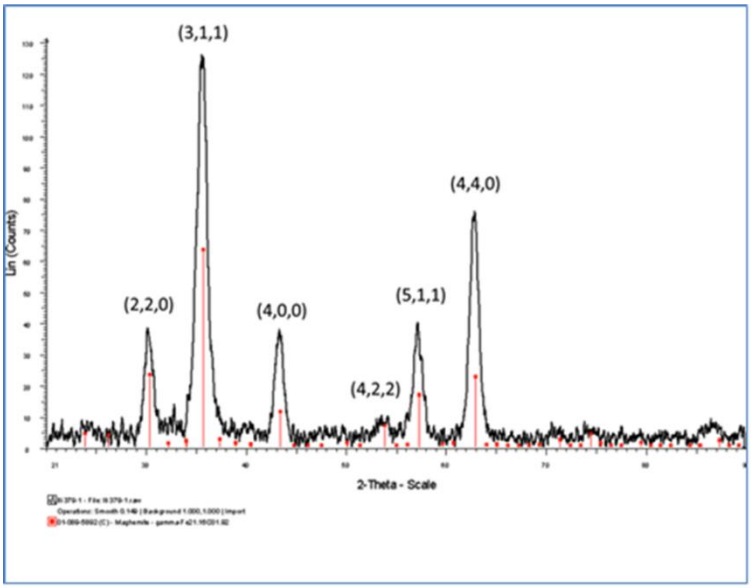

Figure 5: XRD spectrum of ultra-small 6.61±2.04 nm-sized core CAN_{DOE}-γ-Fe_2O_3 NPs

Magnetic properties of CAN_{DOE}-γ-Fe_2O_3 NPs have been also characterized by SQUID analysis (Quantum Design, MPMS XL model operating in a 2 to 400°K temperature range with magnetic fields up to 5.5T, Fig. SI-8, p. SI-8) and MRI relaxivity measurements (Fig. SI-10, p. SI-9). They showed a super-paramagnetic behavior (absence of hysteresis loop) characterized by a saturation magnetization Ms of 75.2 emu/g NPs and a blocking temperature of 109-110°K (Fig. SI-9, p. SI-9, ZFC/FC graphs, H = 100 Oe).

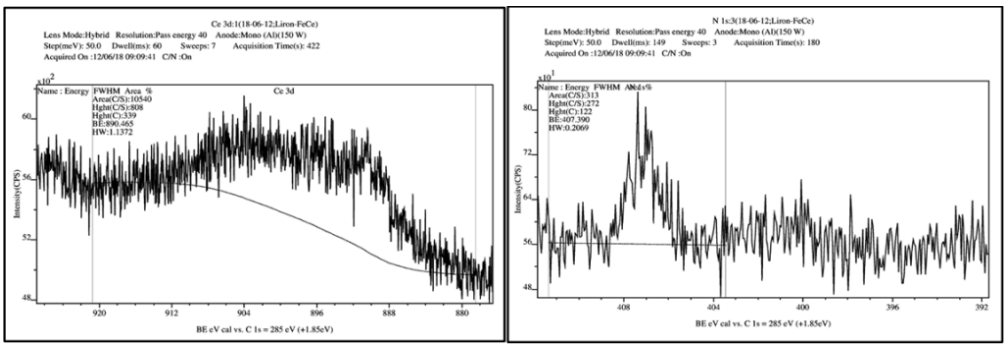

Figure 6: XPS spectroscopy of ultra-small 6.61±2.04 nm-sized core CAN_{DOE}-γ-Fe_2O_3 NPs - Characteristic Ce $3d_{5/2}$ (surface-localized $[Ce^{3/4+}L_n]$ species) & N 1s (L: *complexing nitrate* NO_3^- *anion*) peaks

In addition, MRI r1 and r2* relaxivity measurements for assaying NP effectiveness in contrast enhancement have been performed (7.0 T Bruker Biospec, Bruker Biospin, room temperature). Conventional weighting T1 (RARE) and T2* (Multi Gradient Echo -

MGE) sequences made use of sampling test tubes that contained increasing elemental Fe concentrations (ICP-AES, ddH_2O medium, 0.06, 0.12, 0.25, and 0.5 nmol elemental Fe/tube, Fig. SI-10, p. SI-9). $1/T_1$ and $1/T_{2*}$ relaxation rates varied linearly with Fe concentrations affording longitudinal and transverse r_1 and r_{2*} relaxivity (curve slopes) values of 0.0015 and 189 mmol-1-s-1 respectively as might be expected for strong T_{2*} relaxation maghemite-based NPs.[10, 11, 32]

2.5. *b*-PEI$_{25}$-CAN$_{DOE}$-*γ*-Fe$_2$O$_3$ NPs - siRNA loading and gene silencing results using dual-reporter human osteosarcoma U2OS cells

Quite interestingly for potential applications in the siRNA delivery/cellular gene silencing field, former innovative optimized $[CeL_n]^{3/4+}$ complex-decorated CAN$_{DOE}$-γ-Fe$_2$O$_3$ NPs have been readily surface-modified by contact with a 25kDa branched polycationic b-PEI$_{25}$ polymer (milliQ H_2O, room temperature, b-PEI$_{25}$/Fe w/w ratio: 5.25, optimal experimental protocol, SI section - part C, p. SI-4). This type of branched b-PEI$_{25}$ polymer possesses a quite high positive charge density due to the formation of a dense network of ammonium (R_3N+/RR'NH_2+/NH_3+) cations that enable strong electrostatic capture and condensation of negatively charged siRNA species for cell delivery and gene silencing.[33-37] It is also well known for its strong endosomal escape capability following intracellular uptake ("proton sponge" effect).[37] Thus, further 2nd step surface engineering of former CAN$_{DOE}$-γ-Fe$_2$O$_3$ NPs involved the binding (Lewis acid $[CeL_n]^{3/4+}$ complex-based coordination mode) of polyN-containing Lewis base polymeric b-PEI$_{25}$ that enabled $[CeL_n]^{3/4+}$ complex multi-dentate chelation. Indeed, rapid screening of various b-PEI$_{25}$/elemental Fe w/w ratios provided an optimal (gene silencing) b-PEI$_{25}$/Fe w/w ratio of 5.25 that afforded hydrophilic stable and non-aggregated aqueous suspensions of 6.86±1.55 nm (TEM)-sized b-PEI$_{25}$-CAN$_{DOE}$-γ-Fe$_2$O$_3$ NPs (Fig. SI-11, p. SI-10, DLS size: 82.90±1.26 nm). Interestingly, corresponding b-PEI$_{25}$-CAN$_{DOE}$-γ-Fe$_2$O$_3$ NPs afforded the same 0.1000 w/w Ce/Fe ratio as starting CAN$_{DOE}$-γ-Fe$_2$O$_3$ NPs (ICP-AES measurements). They also disclosed a positive ξ potential value of +31.1 mV (SI section, p. SI-4). This value is significantly lower than the one measured for starting CAN$_{DOE}$-γ-Fe$_2$O$_3$ NPs (+45.7 mV), but it remained highly positive most likely due to the newly bound $[CeL_n]^{3/4+}$ complex-interacting b-PEI$_{25}$ phase. Further confirmation of such a b-PEI$_{25}$-mediated NP surface modification arose from both combined XPS and TGA analyses. XPS analysis (Fig. SI-12, p. SI-10) confirmed the presence of previously observed NP surface interacting NO_3- anions and of the polyamine b-PEI$_{25}$ phase (characteristic N 1s peaks, BE: 406.0-407.0 & 398.0-402.0 eV respectively). On the other hand, thermogravimetric analysis, - TGA thermograms and weight loss derivative function graphs (Fig. SI-7, p. SI-8) provided a quantified insight concerning the NP organic phase composition of b-PEI$_{25}$-CAN$_{DOE}$-γ-Fe$_2$O$_3$ NPs vs. both starting CAN$_{DOE}$-γ-Fe$_2$O$_3$ NPs and pure b-PEI$_{25}$. The b-PEI$_{25}$ phase has been found to account for a 73.62% weight loss for the indicated b-PEI$_{25}$ characterizing 200-410°C temperature range (averaged triplicate measurements). In addition, this bound b-PEI$_{25}$ phase has also caused modifications in both r_1 (increase) and r_{2*} (reduction) MRI relaxivity parameters (0.103 & 168 mmol-1s-1 respectively) toward T_{2*} active maghemite-based NPs as contrast agents.

Then and in a final evaluation step, the biological activity of optimized b-PEI_{25}-CAN_{DOE}-γ-Fe_2O_3 NPs in gene silencing has been tested using a well-known two-gene reporter system based on two luciferase proteins, i.e., 61 and 36 kDa Firefly and Renilla, in stably transfected human osteosarcoma U2OS cells (U2OS-Luc).[38] This dual luciferase system enables measuring specific silencing (Firefly), whereas the Renilla remains unchanged unless tested NPs might show toxicity effects, thus causing cell death and reduction in the enzyme level compared to control (cells untreated with same NPs, Fig. 7 and experimental section).

Subsequently, the down-regulation of the Firefly luciferase was conducted using a constant amount of siRNA (100 nM, 0.166 µg) that was loaded using different [Fe/siRNA]/[b-PEI_{25}/siRNA] w/w ratios. This resulted in six different (0.063/0.493-0.630/4.930) tested w/w ratios (Fig. 7). Gene activities were tested after a 48h treatment using a Dual-Luciferase assay (experimental section), silencing efficacy being reflected by luciferase activities normalized to control luciferase ones. Interestingly, optimal [Fe/siRNA]/[b-PEI_{25}/siRNA] ratios for silencing have been found in a quite low 0.157/1.233-0.315/2.465 range demonstrating almost 100% silencing. Higher [Fe/siRNA]/[b-PEI_{25}/siRNA] w/w ratios showed signs of moderate toxicity as can be seen in the reduction of the Renilla activity level.

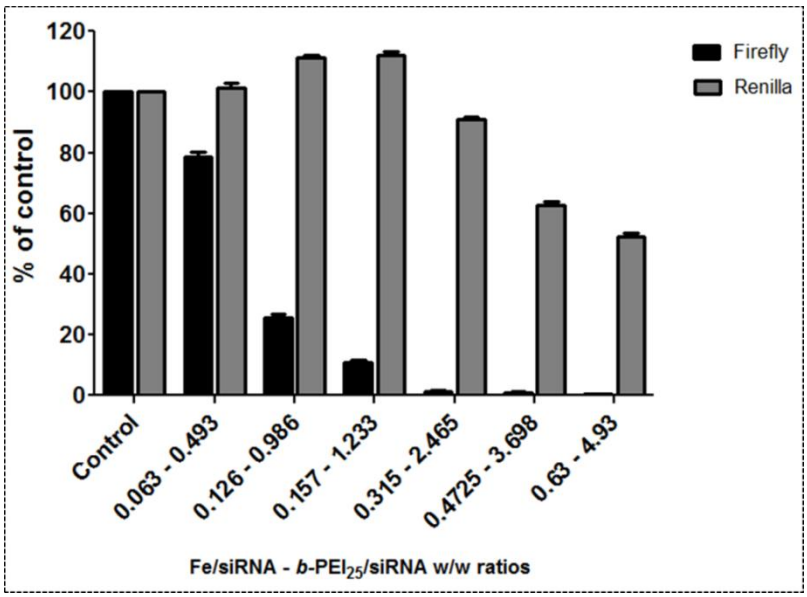

Figure 7: Luciferase silencing using *b*-PEI_{25}-CAN_{DOE}-γ-Fe_2O_3 NPs in U2OS-Luc cells

Conclusions

To the best of our knowledge, this is the first time that a statistical DoE method has ever been used for a globally optimized surface engineering of magnetic ultra-small maghemite (γ-Fe_2O_3) NPs involving positively charged Ce(III/IV) cations (ultrasound-assisted multi-parametric doping process). Beyond effective NP anti-aggregation properties (charge repulsion effects), same NP surface-localized $[CeL_n]^{3/4+}$-complexes also acted as strong Lewis acid centers for the thermodynamically favored coordination attachment of a polycationic branched 25kDa b-PEI_{25} polymer. Resulting fully characterized 6.86±1.55 nm-sized DoE-optimized b-PEI_{25}-CAN_{DOE}-γ-Fe_2O_3 NPs enabled a very effective siRNA loading and cell delivery/gene silencing using a well-known in vitro dual luciferase system (siRNA-mediated gene silencing technology). In summary, this NP platform technology provides a wide range of opportunities for the successful development of additional biocompatible MRI (T2* contrast agent) and/or drug delivery biomedicine applications.

Notes and references

† Electronic Supplementary Information (ESI) available: [This section comprises the corresponding items: detailed experimental procedures for the preparation of (i) starting Massart magnetite (Fe_3O_4) nanoparticles, (ii) CAN_{DOE}-stabilized maghemite nanoparticles (DoE optimization: 2D counter plot graphs & MINITAB® 16 profile optimizer tool data), (iii) b-PEI_{25}-CAN_{DOE}-γ-Fe_2O_3 NPs with NP size distribution histograms, (iv) complete NP characterization data including magnetism features, & a typical NP-mediated siRNA transfection procedure (Firefly Luciferase silencing).].

‡ **Experimental section**

Materials. All the specific chemicals and reagents (analytical grade and/or highest purity level) used in this study, i.e., $FeCl_3$•$6H_2O$, $FeCl_2$•$4H_2O$, NH_4OH (ACS reagent, 28-30%), ceric ammonium nitrate (CAN, $Ce^{IV}(NH_4)_2(NO_3)_6$), fluorescein isothiocyanate (FITC ≥ 90% HPLC), dipicolinic acid (Dpic), branched polyethyleneimine (b-PEI_{25}, MW ≈ 25kDa) have been purchased from Sigma-Aldrich (Israel) and have been used without any further purification. The Dulbecco's Modified Eagle Medium (DMEM) supplemented with 10% fetal bovine serum, 25mM HEPES, as well as both penicillin-streptomycin amphotericin B, and L-glutamine solutions (29.2 mg/ml in saline - 200 millimoles/liter) have been purchased from Biological Industries Ltd. (Israel). The double-stranded oligonucleotide sequence (sense/antisense) used for Luciferase knock-down (5'-GGACAUCACCUAUGCCGAGUACUTC-3'/5'-CACCUGUAGUGGAUACGGCUCAUGAAG-3') was obtained from QBI Enterprises Ltd. (Ness Ziona, Israel). The Dual-Glo® Luciferase Assay System was from Promega (Madison, WI, USA) while LysoTracker® Red DND-99 was purchased from Invitrogen (Carlsbad, CA, USA).

Methods. X-ray photoelectron (XPS), FT-IR, and inductively coupled plasma atomic emission (ICP-AES) spectroscopies as well as thermogravimetric (TGA), and X-ray powder diffraction (XRD) analyses requested the preparation of dry powder samples (vacuum stove 1h at 40°C followed by lyophilization using a FreeZone 2.5 liter bench-top freeze dry system, - Labconco, Kansas City, MO, USA). High-power ultrasonication reactions were conducted using a high-power ultrasonicator (Sonics®, Vibra cell, 750 Watt, power modulator set-up at 25%)

equipped with a titanium horn under an argon atmosphere. Samples for low and high-resolution TEM analyses were prepared by spreading a small drop of aqueous maghemite-based nanoparticle dispersions on amorphous carbon-coated copper grids (Formvar carbon 400 mesh grids, SPI® Supplies West Chester, USA) followed by air-drying.

Transmission Electron Microscopies at low and high resolutions (TEM/HR-TEM) made use of both JEM 1400 and 2100 (JEOL USA Inc.) microscopes (200 kV acceleration voltage, 2x2k & 4x4k CCD cameras respectively).

FT-IR spectra were recorded using a Bruker TENSOR 27 spectrometer (Diffuse Reflectance Accessory EasyDiff, PIKE Technologies, 4 cm^{-1} resolution). Samples were prepared by mixing NPs powders with dry IR grade KBr (2% weight).

DLS (hydrodynamic NP average diameter) and ξ potential measurements have been performed using (i) a Zetasizer Nano-ZS (Malvern Instruments Ltd, UK) employing a nominal 5mW He-Ne laser (operating wavelength: 633 nm, 20°C, triplicate measurements), and (ii) disposable DTS1060C-Cleare ξ cells (ddH_2O, 25°C).

ICP-AES elemental analyses have been run using a ULTIMA 2 spectrometer (HORIBA, Jobin Yvon Inc.).

X-ray powder diffraction (XRD) patterns have been obtained using a Bruker AXS D8 Advance diffractometer (Bragg-Brentano geometry, Cu-K_α radiation: λ = 1.54Å) operated at 40kV/40 mA. XRD 2Ø measurements were performed in a 20 to 80° range (step size of 0.05° at a 0.5 sec/step rate).

Surface-sensitive X-ray photoelectron spectroscopy (XPS) analyses have been executed using a Kratos Axis HS apparatus equipped with a Kratos "Vision 2" package software. NPs samples deposited onto a double-sided carbon-based self-adhesive tape (complete coverage) were loaded in a ultra-high vacuum chamber (5×10^{-10} Torr).

Thermogravimetric analyses (TGA) have been processed using a TGA/DSC1 analyzer (N_2 atmosphere/50 mL/min at a heating rate of 10°C/min, Mettler-Toledo, OH, USA). Dry NPs samples (8-10 mg) afforded TGA thermograms and corresponding weight loss derivative function graphs in a 25-850°C temperature range.

Magnetism (saturation magnetizations Ms, coercivity factors Hc including ZFC/FC graphs/H = 100 Oe) analyses have been obtained using a SQUID Quantum Design magnetometer (MPMS XL model operated in a 2 to 400°K temperature range with magnetic fields up to 5.5T).

MRI r1 and r2* relaxivity measurements have been conducted at room temperature on a 7.0 T Bruker Biospec instrument (Bruker Biospin) using conventional weighting T1 (RARE) and T2* (Multi Gradient Echo - MGE) sequences.

siRNA transfection experiments - Firefly Luciferase silencing

U2OS luciferase expressing cells (U2OS-Luc) were seeded at $1x10^4$ cells/well in 100 μL medium in a 96 well optical bottom plate (Thermo) and incubated overnight at 37°C with 5% CO_2. Cells were transfected with *Firefly* luciferase siRNA (resuspended in milliQ purified H_2O in acordance with the manufacturer instructions) at a concentration of 100 nM (0.166 µg) mixed with optimal ***b*-PEI$_{25}$-CAN$_{DOE}$-γ-Fe$_2$O$_3$ NPs** (dispresed in milliQ purified H_2O) at different [Fe/siRNA]/[*b*-PEI$_{25}$/siRNA] w/w ratios (0.063-0.493, 0.126-0.986, 0.157-1.233, 0.315-2.465, 0.4725-3.698 and 0.630-4.930). The siRNA and NPs suspentions were incubated for 15 minutes at room temperature and then added to the cells. Untreated cells were used as control.

The following oligonucleotide sequences (sense/antisense) were used: **5'-GGACAUCACCUAUGCCGAGUACUTC-3'/5'-CACCUGUAGUGGAUACGGCUCAUGAAG-3'**. Forty-eight hours later, cells were assayed for both *Firefly* and *Renilla* luciferase activities using the Dual-GLO® Luciferase Assay System (Promega). Briefly, cells were lysed and the *Firefly* luciferase substrate added (50 μL per well Dual-GLO® Substrate/Buffer). After 10 min, the *Firefly* luciferase activity was measured using a luminometer device (Synergy 4, Biotek). Next,

the *Renilla* luciferase substrate was added (50 μL per well Stop & GLO® Substrate/Buffer) and the luminescence measured after additional 10 min incubation. Then, silencing efficacy is quantified by luciferase activities normalized to control luciferase activities.

References

1. Gautam, A.; van Veggel, F. C. J. M., Synthesis of Nanoparticles, their Biocompatibility, and Toxicity Behavior for Biomedical Applications. *J. Mater. Chem. B* **2013,** *1*, 5186-5200.
2. Han, N.; Yang, Y. Y.; Wang, S.; Zheng, S.; Fan, W., Polymer-Based Cancer Nanotheranostics: Retrospectives of Multi-Functionalities and Pharmacokinetics. *Curr. Drug Metab.* **2013,** *14*, 661-674.
3. Pablico-Lansigan, M. H.; Situ, S. F.; Samia, A. C. S., Magnetic Particle Imaging: Advancements and Perspectives for Real-Time in vivo Monitoring and Image-Guided Therapy. *Nanoscale* **2013,** *5*, 4040-4055.
4. Lam, T.; Pouliot, P.; Avti, P. K.; Lesage, F.; Kakkar, A. K., Superparamagnetic Iron Oxide Based Nanoprobes for Imaging and Theranostics. *Adv. Colloid Interface Sci.* **2013,** *199-200*, 95-113.
5. Mok, H.; Zhang, M., Superparamagnetic Iron Oxide Nanoparticle-Based Delivery Systems for Biotherapeutics. *Expert Opin. Drug Delivery* **2013,** *10*, 73-87.
6. Hilger, I.; Kaiser, W. A., Iron Oxide-Based Nanostructures for MRI and Magnetic Hyperthermia. *Nanomedicine* **2012,** *7*, 1443-1459.
7. Niemirowicz, K.; Markiewicz, K. H.; Wilczewska, A. Z.; Car, H., Magnetic Nanoparticles as New Diagnostic Tools in Medicine. *Adv. Med. Sci.* **2012,** *57*, 196-207.
8. Sutphin, P. D.; Flores, E. J.; Harisinghani, M., Magnetic Nanoparticles in Magnetic Resonance Imaging and Drug Delivery. *Drug Delivery Oncol.* **2012,** *1*, 225-245.
9. Wahajuddin; Arora, S., Superparamagnetic Iron Oxide Nanoparticles: Magnetic Nanoplatforms as Drug Carriers. *Int. J. Nanomed.* **2012,** *7*, 3445-3471.
10. Zhang, R.; Olin, H., Magnetic Nanoparticles in Biomedical Applications. *OMICS Biomed. Perspect. Appl.* **2012**, 119-139.
11. Gossuin, Y.; Gillis, P.; Hocq, A.; Vuong, Q. L.; Roch, A., Magnetic Resonance Relaxation Properties of Superparamagnetic Particles. *Wiley Interdiscip. Rev. Nanomed. Nanobiotechnol.* **2009,** *1*, 299-310.
12. Petri-Fink, A.; Hofmann, H., Superparamagnetic Iron Oxide Nanoparticles (SPIONs): from Synthesis to in vivo Studies - A Summary of the Synthesis, Characterization, in vitro, and in vivo Investigations of SPIONs with Particular Focus on Surface and Colloidal Properties. *IEEE Trans. Nanobioscience* **2007,** *6*, 289-297.
13. Haviv, A. H.; Greneche, J.-M.; Lellouche, J.-P., Aggregation Control of Hydrophilic Maghemite (□-Fe_2O_3) Nanoparticles by Surface Doping Using Cerium Atoms. *J. Am. Chem. Soc.* **2010,** *132*, 12519-12521.
14. Deleersnyder, K.; Schaltin, S.; Fransaer, J.; Binnemans, K.; Parac-Vogt, T. N., Ceric Ammonium Nitrate (CAN) as Oxidizing or Nitrating Reagent for Organic Reactions in Ionic Liquids. *Tetrahedron Lett.* **2009,** *50*, 4582-4586.
15. Dhakshinamoorthy, A.; Pitchumani, K., Clay-Supported Ceric Ammonium Nitrate as an Effective, Viable Catalyst in the Oxidation of Olefins, Chalcones and Sulfides by Molecular Oxygen. *Catal. Commun.* **2009,** *10*, 872-878.

16. Nuran, I.; Fatma, K.; Murat, I., Graft Copolymerization of Itaconic Acid onto Sodium Alginate using Ceric Ammonium Nitrate as Initiator. *J. Appl. Polym. Sci.* **2009,** *114*, 40-48.
17. Karraker, D. G., Coordination of Trivalent Lanthanide Ions. *J. Chem. Educ.* **1970,** *47*, 424-430.
18. Limaye, S. N.; Saxena, M. C., Relative Complexing Tendencies of Oxygen-Oxygen, Oxygen-Nitrogen, and Oxygen-Sulfur Donor (Secondary) Ligands in Some Lanthanide-EDTA Mixed-Ligand Complexes. *Can. J. Chem.* **1986,** *64*, 865-870.
19. Arnold, P. L.; Casely, I. J.; Zlatogorsky, S.; Wilson, C., Organometallic Cerium Complexes from Tetravalent Coordination Complexes. *Helv. Chim. Acta* **2009,** *92*, 2291-2303.
20. Aghabozorg, H.; Roshan, L.; Firoozi, N.; Bagheri, S.; Ghorbani, Z.; Kalami, S.; Mirzaei, M.; Shokrollahi, A.; Ghaedi, M.; Aghaei, R.; Ghadermazi, M., Syntheses, Crystal, and Molecular Structures of Mn(II), Zn(II), and Ce(III) Compounds and Solution Studies of Mn(II), Ni(II), Cu(II), Zn(II), Cd(II), and Ce(III) Compounds Obtained from a Suitable Proton Transfer Compound Containing bda and pydcH2 (bda = butane-1,4-diamine; pydcH2 = pyridine-2,6-dicarboxylic acid). *Struct. Chem.* **2010,** *21*, 701-714.
21. Edelmann, F. T., Lanthanides and Actinides: Annual Survey of their Organometallic Chemistry Covering the Year 2009. *Coord. Chem. Rev.* **2012,** *256*, 1151-1228.
22. Cawse, J. N., Experimental Strategies for Combinatorial and HighThroughput Materials Development. *Acc. Chem. Res.* **2001,** *34*, 213.
23. Lendrem, D.; Owen, M.; Godberts, S., DOE (Design of Experiments) in Development Chemistry: Potential Obstacles. *Org. Process Res. Dev.* **2001,** *5*, 324-326.
24. McKay, B.; Hoogenraad, M.; Damen, E. W. P.; Smith, A. A., Advances in Multivariate Analysis in Pharmaceutical Process Development. *Curr. opin. Drug Discovery Dev.* **2003,** *6*, 966-977.
25. Kenett, R.S. and Zacks, S. with contributions by Amberti, D. *Modern Industrial Statistics: with applications in R, MINITAB and JMP*, 2nd ed.; John Wiley and Sons, Chichester, 2014.
26. Prasad, T. K.; Rajasekharan, M. V., A Novel Water Octamer in Ce(dipic)(2)(H2O)(3)•4H(2)O: Crystallographic, Thermal, and Theoretical Studies. *Cryst. Growth Des.* **2006,** *6*, 488-491.
27. Katada, H.; Seino, H.; Mizobe, Y.; Sumaoka, J.; Komiyama, M., Crystal Structure of Ce(IV)/Dipicolinate Complex as Catalyst for DNA Hydrolysis. *J. Biol. Inorg. Chem.* **2008,** *13*, 249-255.
28. Kim, J.-H.; Lee, S.; Kim, K.; Jeon, H.; Park, R.-W.; Kim, I.-S.; Choi, K.; Kwon, I. C., Polymeric Nanoparticles for Protein Kinase Activity. *Chem. Comm.* **2007**, 1346-1348.
29. Sjoeback, R.; Nygren, J.; Kubista, M., Absorption and Fluorescence Properties of Fluorescein. *Spectrochim. Acta, Part A* **1995,** *51A*, L7-L21.
30. Baltrusaitis, J.; Schuttlefield, J.; Jensen, J. H.; Grassian, V. H., FTIR Spectroscopy Combined with Quantum Chemical Calculations to Investigate Adsorbed Nitrate on Aluminium Oxide Surfaces in the Presence and Absence of Co-Adsorbed Water. *Phys. Chem. Chem. Phys.* **2007,** *9*, 4970-4980.
31. Sarin, V. K.; Kent, S. B. H.; Tam, J. P.; Merrifield, R. B., Quantitative Monitoring of Solid-Phase Peptide-Synthesis by the Ninhydrin Reaction. *Anal. Biochem.* **1981,** *117*, 147-157.
32. Rudzka, K.; Delgado, A. V.; Viota, J. L., Maghemite Functionalization for Antitumor Drug Vehiculization. *Mol. Pharmaceutics* **2012,** *9*, 2017-2028.
33. Vicennati, P.; Giuliano, A.; Ortaggi, G.; Masotti, A., Polyethylenimine in Medicinal Chemistry. *Curr. Med. Chem.* **2008,** *15*, 2826-2839.

34. Uchegbu, I. F.; Dufes, C.; Kan, P. L.; Schatzlein, A. G., Polymers and Dendrimers for Gene Delivery in Gene Therapy. *Gene Cell Ther. (3rd Ed.)* **2009**, 321-339.

35. Nimesh, S., Polyethylenimine as a Promising Vector for Targeted siRNA Delivery. *Curr. Clin. Pharmacol.* **2012,** *7*, 121-130.

36. Lee, Y.; Kataoka, K., Delivery of Nucleic Acid Drugs. *Adv. Polym. Sci.* **2012,** *249*, 95-134.

37. Kwon, Y. J., Before and After Endosomal Escape: roles of Stimuli-Converting siRNA/Polymer Interactions in Determining Gene Silencing Efficiency. *Acc. Chem. Res.* **2012,** *45*, 1077-1088.

38. Staplin, W. R.; Miller, W. A., In vivo Analyses of Viral RNA Translation. *Methods Mol. Biol. (Totowa, NJ, U.S.)* **2008,** *451*, 99-112.